Online Magnetometer Calibration in Indoor Environments for Magnetic field-based SLAM

Jade Coulin, Richard Guillemard, Vincent Gay-Bellile, Cyril Joly, Arnaud de La Fortelle

Online Magnetometer Calibration in Indoor Environments for Magnetic field-based SLAM

Jade Coulin[1,2⋆], Richard Guillemard[1], Vincent Gay-Bellile[1], Cyril Joly[2] and Arnaud de La Fortelle[2]

***Abstract*—This paper proposes a new process for calibrating a magnetometer in indoor environments that is accurate, easily deployable and time efficient. Our approach simultaneously estimates the calibration of the magnetometer with the local variations of the magnetic field modeled by a Gaussian Process. To guarantee an accurate estimation of the magnetometer calibration, a two-step optimization algorithm is proposed. Experiments show that the proposed solution is as accurate as outdoor calibration algorithms, and more precise than state-of-the-art indoor calibration methods.**

***Index Terms*—Magnetometer, calibration, non-linear optimization.**

I. INTRODUCTION

Traditionally, magnetometers are used in outdoor environments to determine the heading of a system. The high variability of the indoor magnetic field was considered as chaotic, with no predictable patterns, and therefore has not been exploited in indoor localization algorithms until a few years ago. However, recent work considers indoor magnetic perturbations as an asset rather than a drawback as they are temporally stable and spatially contrasted [1]. Thus many indoor localization approaches exploiting magnetic field have been proposed in the last 10 years ([2], [3]). Recently, [4] demonstrates that using a magnetic map rather than a visual one in Visual-Inertial Simultaneous Localization and Mapping (VISLAM) algorithms give better results for long-term indoor localization. In [3], a magnetic field-based SLAM algorithm building online a magnetic map is proposed. It results in accurate localization when the trajectory regularly passes by the same places.

However, magnetic field-based localization algorithms assume that the magnetometer is perfectly calibrated beforehand. Its calibration changes over time, so it must be recalibrated regularly. The recalibration procedure must therefore be easy to implement in order to facilitate the deployment of magnetic field-based localization solutions. The most commonly used method is to calibrate the magnetometer outdoors, as far away as possible from any metal structures that disturb the Earth's magnetic field ([5], [6]). As these conditions are difficult to obtain in dense urban areas, different indoor calibration procedures have been proposed.

In [7], they propose to simultaneously estimate the calibration of the magnetometer and the local variations of the magnetic field by nonlinear optimization. Even if this approach seems promising, it presents some limitations. Firstly, the magnetic field variations are modeled by splines, without taking into account the physical properties of the magnetic field. This results in poorly accurate calibration. Secondly, their approach is not easily deployable since it uses a motion capture system to estimate the poses of the magnetometer as it is moved and rotated in all directions.

In this paper, we propose a solution to accurately calibrate a magnetometer in an indoor environment that is easily deployable and time efficient. To this end, we propose several improvements to the approach described in [7]. Firstly, to improve the accuracy of the calibration estimate, we take advantage of the physical properties of the magnetic field by modeling its variations through a Gaussian Process (GP) on the scalar potential of the magnetic field. Then, to make our calibration procedure easily deployable, the magnetometer is mounted with cameras and an inertial sensor. The poses of the magnetometer are estimated by a VISLAM algorithm. Finally, to guarantee an accurate and efficient estimation of the calibration, a two-step optimization algorithm is proposed. In the first step, a coarse calibration is estimated assuming that the magnetic field is locally constant. At this step, the input data (i.e. the magnetic data with their associated poses) are analyzed to determine if all the calibration parameters are sufficiently well constrained. In the second step, the magnetometer calibration is refined by simultaneously estimating the variations of the magnetic field through non linear optimization. We demonstrate experimentally that the calibration accuracy estimated by our approach is close to a calibration performed outdoors and more accurate than the one from [7]. We also evaluate the impact of the calibration on the localisation accuracy of a magnetic field-based SLAM [3].

This paper is structured as follows. Section II presents a review of the existing magnetometer calibration algorithms. A brief presentation of the magnetometer model and magnetic field modeling through GP is presented in Section III. Our calibration algorithm is explained in Section IV and evaluated in Section V. It is compared with the calibration algorithm proposed in [7].

II. RELATED WORK

Magnetometer calibration is the estimation of its bias and its scale-misalignment matrix. The most common methods for magnetometer calibration require a constant magnetic field. This condition is verified outdoors, far from any buildings or metallic objects where the measured magnetic field is equal to the Earth magnetic field. Therefore the magnetometer calibration has been extensively studied outdoor ([5], [6], [8], [9]). Outdoor calibration algorithms generally require rotating the magnetometer in as many directions as possible ([6], [8], [10], [11]). The collected uncalibrated magnetic measures form an

ellipsoid with a center shifted from (0;0;0). Accurate values for the scale-misalignment and the bias of the magnetometer are estimated by fitting this ellipsoid to a sphere whose center is (0;0;0).

On the other hand, indoor, the magnetometer calibration is more challenging since the field is not known a priori and is subject to numerous spatial fluctuations caused by the ferromagnetic elements in the building structure, i.e. steel pillars, metallic tubs. In [10], inertial sensors are used to improve the robustness of magnetometer calibration when it is mounted on a system distorting the magnetic field. This approach may theoretically be applied indoor since it does not require the norm and direction of the real field for the calibration. However, in practice it requires a constant magnetic field which is rarely the case indoors [2].

In [12], the calibration of the magnetometer is estimated at the same time as its localization from a pre-existing magnetic map. While this approach enables to avoid recalibration of the magnetometer before using it for localization purposes, an outdoor calibration of the magnetometer must be performed at each magnetic map building. To overcome this limitation, the authors propose a solution to build a magnetic map without accurate calibration of the magnetometer. They assume that at each position the calibrated magnetic measurements are unique. This assumption is false for magnetic measurements acquired at the same location with different orientations when the magnetometer calibration is inaccurate.

Instead of using a pre-build magnetic map, in [7], the magnetometer calibration is tightly coupled with the creation of a magnetic map. Their main idea consists in a simultaneous estimation of the magnetometer calibration parameters and a magnetic field model through non linear optimization algorithm. They use splines for modeling the variation of the magnetic field. It results in defective accurate calibration since the physical properties of the magnetic field are not taken into account. Furthermore, they use motion capture equipment to estimate the poses of the magnetometor during the calibration acqusition, making their solution not easily deployable.

III. MAGNETOMETER MODEL AND MAGNETIC FIELD MODELING

In this section, we introduce the basic elements necessary for our magnetometer calibration algorithm. First, the magnetometer model and its calibration parameters are presented. Then, the modeling of the magnetic field variations by a Gaussian process is briefly summarized.

A. Magnetometer model

The magnetometer measurements are corrupted by several types of error: some are due to imperfections of the sensor itself and others to the acquisition system it is mounted on. The sensor itself suffers from a bias $\mathbf{b}_S$ and of a scaling factor $\mathbf{A}_S$ on its measures, as well as a white noise $\boldsymbol{\eta}$. The acquisition system also distorts the measured magnetic field via its metallic and electronic components. Thus, the calibration must be performed with the magnetometer already integrated on the acquisition platform. In our case, the targeted application is indoor localization by magneto-visual-inertial SLAM: the cameras, the Inertial Measurement Unit (IMU) and the magnetometer must all be mounted together during the calibration of the magnetometer. The disturbances of the magnetic field related to the acquisition system are modeled as follows: the hard iron effects correspond to a constant additional magnetic field $\mathbf{b}_{HI}$, while the soft iron effects, described by a scale matrix $\mathbf{A}_{SI}$, characterize the distortions of the field which are orientation-dependent. Moreover the alignment of the axis of the magnetometer is imperfect, causing another bias on the measures $\mathbf{b}_{align}$.

Let's note G the global reference frame, and B the body frame associated to the magnetometer. As B changes over time, it is indexed by its corresponding timestamp number, n. $\mathrm{R}_{B_nG} \in SO(3)$ is the rotation matrix of B_n from the frame G.

The magnetometer measure $\hat{\mathbf{m}}_{B_n}$ in the frame B_n verifies therefore the following equation:

$$\begin{aligned}\hat{\mathbf{m}}_{B_n} &= \mathbf{A}_S(\mathbf{A}_{SI}\mathbf{m}_{B_n} + \mathbf{b}_{HI} + \mathbf{b}_{align}) + \mathbf{b}_S + \boldsymbol{\eta} \\ &= \mathbf{A}_S(\mathbf{A}_{SI}\mathrm{R}_{B_nG}\mathbf{m}_G + \mathbf{b}_{HI} + \mathbf{b}_{align}) + \mathbf{b}_S + \boldsymbol{\eta} \\ \text{with } \boldsymbol{\eta} &\sim \mathcal{N}(\mathbf{0}, \sigma_m^2\mathbf{I}_3)\end{aligned} \tag{1}$$

with $\mathbf{m}_{B_n}$, $\mathbf{m}_G$ the real magnetic field expressed in the body frame B_n, the global reference frame G respectively and σ_m the amplitude of the Gaussian random white noise $\boldsymbol{\eta}$.

Equation 1 can be simplified as:

$$\begin{aligned}\hat{\mathbf{m}}_{B_n} &= \mathbf{A}\mathrm{R}_{B_nG}\mathbf{m}_G + \mathbf{b}_m + \boldsymbol{\eta} \\ \text{with } \boldsymbol{\eta} &\sim \mathcal{N}(\mathbf{0}, \sigma_m^2\mathbf{I}_3)\end{aligned} \tag{2}$$

where $\mathbf{A}$ is a scale-misalignment matrix and $\mathbf{b}_m$ is the magnetometer bias. σ_m^2 is estimated by a motionless acquisition of the acquisition system [13]. The magnetometer model may also include a random walk noise but, according to the Allan variance of the sensor, it is negligible for acquisitions of a few hours. In the long term it corresponds to a progressive shift of the bias $\mathbf{b}_m$ and therefore can be omitted from the equations ([13], [4]).

The proposed calibration algorithm described in Section IV estimates $\mathbf{A}$ and $\mathbf{b}_m$, the magnetometer intrinsics. The diagonal coefficients of $\mathbf{A}$ correspond to the scale and its non-diagonal coefficients to misalignment. $\mathbf{A}$ is a symmetric matrix, with 6 DoF. As all the parameters in an indoor environment are observable up to an unknown scale factor, one of the scale parameters must be fixed: its value is obtained once and for all with a unique outdoor calibration. Therefore there is a total of 8 unknown calibration parameters.

B. Magnetic field modeling

Our magnetometer calibration algorithm is based on the simultaneous estimation of the magnetic field variation. We use Gaussian Process regression on the scalar potential of the magnetic field ([14]) to take into account its physical properties.

The magnetic field is a vector field that associates at each point $\mathbf{p}_i$ in space a magnetic value $B(\mathbf{p}_i)$, with $B : \mathbb{R}^3 \to \mathbb{R}^3$.

Applying Maxwell's equations, under the assumption that the free current is negligible, B can be estimated through a unique GP regression, as it is the gradient of a scalar potential φ:

$$B = -\nabla\varphi. \tag{3}$$

Let $\mathbf{p}$ a set of positions where the magnetic field is measured and $\mathbf{x}$ a set of D positions where the magnetic field has to be predicted. Let $\mathbb{E}[B(\mathbf{x})] = [\mathbb{E}[B(\mathbf{x}_1)]^\top, ..., \mathbb{E}[B(\mathbf{x}_D)]^\top]^\top$ be the vector contatening all the predictions of the magnetic field by the GP. From [14], the conditional mean of the magnetic field B for all positions in $\mathbf{x}$, are given by:

$$\mathbb{E}[B(\mathbf{x})] \approx \nabla\Phi_* \Omega \mathrm{vec}(\mathbf{m}), \tag{4}$$

$$\text{with } \Omega = ([\nabla\Phi]^\top \nabla\Phi + \sigma_m^2 \Lambda^{-1})^{-1} [\nabla\Phi]^\top. \tag{5}$$

For simplification $\Phi_* = \Phi(\mathbf{x})$, $\Phi = \Phi(\mathbf{p})$. $\Phi(\mathbf{p})$ is a matrix of size $(N+3) \times 3M$, concatenating all the values of the N eigenfunctions chosen to describe the field at the $\mathbf{p}$ positions (with M the number of positions). $\Phi(\mathbf{x})$ is the matrix of size $(N+3) \times 3D$ concatening the values of the eigenfunctions at the $\mathbf{x}$ positions (see [14] for the explicit expression of $\Phi(\mathbf{p})$, $\Phi(\mathbf{x})$ and of Λ). $\mathrm{vec}(\mathbf{m})$ is a vectorization of all the magnetic measures at $\mathbf{p}$ ordered by their index.

IV. ESTIMATION OF THE MAGNETOMETER CALIBRATION PARAMETERS

Our magnetometer calibration algorithm is described in this section. After a brief overview presented in section IV-A, the two steps of our calibration process are detailed in section IV-B and IV-C.

A. Overview of the proposed magnetometer calibration algorithm

Our calibration algorithm is a two-step process taking as input magnetic data with their associated poses. They are obtained from VISLAM algorithm by mounting the magnetometer together with an IMU sensor and cameras. VISLAM algorithms are the actual state of-the-art methods for indoor localization and they do not rely on costly instrumentation of the environment. The key-frames VISLAM algorithm described in [15] is used in our experiments. To guarantee an accurate pose for each magnetic data, IMU data integration between the key frames poses is performed.

The first step of our calibration process estimates a coarse calibration under the assumption that the magnetic field is locally constant while determining whether the collected data are sufficiently varied in terms of poses to constrain the calibration. This calibration step is based on the fact that two magnetic field measurements acquired at the same location must physically measure the same field. Due to the magnetometer orientation and errors in calibration this is not the case in practice. We demonstrate in Section IV-B that the calibration errors are observable from pairs of magnetic measurements acquired at the same location with different orientations and then expressed in the global reference frame. In practice, these pairs are made up of data acquired close to each other (of the order of a few centimeters), the magnetic field being assumed to be very locally constant. The acqusition of magnetic measurements is stoped when a sufficient number of pairs guaranteeing an accurate calibration is reached as described in Section IV-B3.

The second step of our calibration process refines the calibration obtained in the first step by lifting the assumption that the magnetic field is locally constant. For this purpose, the magnetic field variations modelled by a Gaussian process (Section III-B) are simultaneously estimated with the magnetometer calibration by a non-linear optimisation algorithm. We demonstrate in Section IV-C that this optimization problem can be reformulated to depend only on the calibration parameters.

An overview of the proposed calibration algorithm is presented on Figure 1.

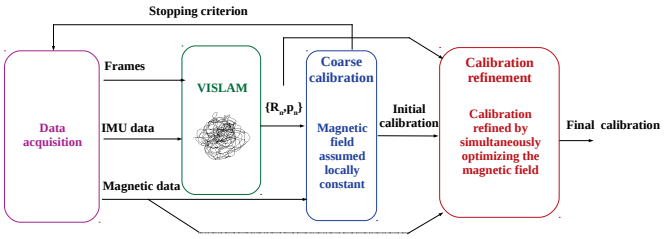

Fig. 1. Overview of our magnetometer calibration process.

B. First step of our calibration process : coarse calibration

To evaluate the magnetometer intrinsics, we propose to compare pairs of magnetic measurements. collected at close positions in space and with different orientations of the sensor. These pairs are formed from a k-nearest neighbor algorithm by selecting the candidate with the highest rotation among the k candidates.

The proposed algorithm for the coarse estimation of the magnetometer calibration alternates the estimation of the bias (the scale misalignment matrix is fixed) and the estimation of the scale misalignment matrix (the bias is fixed) until convergence. The initial value of $\mathbf{A} = \mathbf{I}_3$.

1) Estimation of the bias: Let a pair of magnetic measurements $(\hat{\mathbf{m}}_{B_1}, \hat{\mathbf{m}}_{B_2})$ acquired at almost the same location. $\mathrm{R}_{B_1B_2} \in SO(3)$ is the rotation matrix obtained from the orientations of the magnetometer R_{B_1G} et R_{B_2G}. $\mathbf{m}_{B_1}$ and $\mathbf{m}_{B_2}$ are the real values of the magnetic field that would have been measured by an ideal sensor. The relation between these two values under the assumption that the magnetic field is locally constant is given by:

$$\mathbf{m}_{G_1} = \mathbf{m}_{G_2} \Rightarrow \mathbf{m}_{B_1} = \mathrm{R}_{B_1B_2} \mathbf{m}_{B_2} \tag{6}$$

Using Equation 2, this equality becomes:

$$\mathbf{A}^{-1}(\hat{\mathbf{m}}_{B_1} - \mathbf{b}_m - \boldsymbol{\eta}_1) = \mathrm{R}_{B_1B_2} \mathbf{A}^{-1}(\hat{\mathbf{m}}_{B_2} - \mathbf{b}_m - \boldsymbol{\eta}_2) \tag{7}$$

Since η_1 and η_2 have similar distributions and $\mathrm{R}_{B_1B_2}\mathbf{A}^{-1}$ is close to a rotation matrix, the two noise components of

Equation 7 may be considered to be equal. Equation 7 is then simplified as follows:

$$\mathbf{A}^{-1}(\mathrm{R}_{B_1B_2}-\mathbf{I}_3)\mathbf{b}_m = \mathrm{R}_{B_1B_2}\mathbf{A}^{-1}\hat{\mathbf{m}}_{B_2} - \mathbf{A}^{-1}\hat{\mathbf{m}}_{B_1}. \quad (8)$$

By concatening equations for all the collected pairs of magnetic data and by assuming $\mathbf{A}$ to be known, the bias of the magnetometer is obtained by resolving a linear sytem.

One may observe that if the two magnetic measures are acquired with opposite directions, the left side of the equation 8 is equal to $-2\mathbf{A}^{-1}\mathbf{b}_m$, while if the rotation is small, it is close to 0. For the latter case, the assumption that the noise can be neglected is not verified.

A ponderation weight is thus applied to the equation 8: it is of the form $\exp(-\frac{(\theta_b^{opt}-\theta_{\mathrm{R}_{B_1B_2}})^2}{\Theta^2})$. $\theta_{\mathrm{R}_{B_1B_2}}$ is the absolute value of the rotation angle, between 0 and π: $\theta_{\mathrm{R}_{B_1B_2}} = \arccos\left(\frac{(tr(\mathrm{R}_{B_1B_2})-1)}{2}\right)$ with $tr(\mathrm{R}_{B_1B_2})$ the trace of the matrix. Θ is a parameter that sets the degree of influence regarding to angle difference.

2) Estimation of the scale-misalignment matrix: The estimation of the scale-misalignement matrix can be divided in two parts: the estimation of its scale component (i.e. its diagonal) first and the misalignment coefficients. $\mathbf{A}$ is usually close to the identity matrix: the scale coefficients are close to 1 and the misalignment should be close to 0 for a correctly manufactured sensor. The three diagonal parameters will be represented by $1+s_1$, $1+s_2$ and $1+s_3$ and the alignment ones by t_1, t_2 and t_3 such as:

$$\mathbf{A} = \begin{bmatrix} 1+s_1 & t_1 & t_2 \\ t_1 & 1+s_2 & t_3 \\ t_2 & t_3 & 1+s_3 \end{bmatrix} \quad (9)$$

with s_1, s_2, s_3, t_1, t_2, $t_3 \ll 1$. In the following, s_3 is fixed as mentioned in subsection III-A.

We can write $\mathbf{A} = \mathbf{I}_3 + \lfloor\mathbf{S}\rfloor_D + \lfloor\mathbf{T}\rfloor_S$ with $\mathbf{S} = \begin{bmatrix} s_1 \\ s_2 \\ s_3 \end{bmatrix}$ and $\mathbf{T} = \begin{bmatrix} t_1 \\ t_2 \\ t_3 \end{bmatrix}$. The operator $\lfloor\cdot\rfloor_D$ and $\lfloor\cdot\rfloor_S$ are given by:

$\lfloor\cdot\rfloor_D : \mathbb{R}_3 \to \mathbb{R}_{3\times3}$ and $\lfloor\cdot\rfloor_S : \mathbb{R}_3 \to \mathbb{R}_{3\times3}$.

$$\begin{aligned} &\lfloor\cdot\rfloor_D : \mathbb{R}_3 \to \mathbb{R}_{3\times3} \\ &\left\lfloor \begin{bmatrix} a \\ b \\ c \end{bmatrix} \right\rfloor_D = \begin{bmatrix} a & 0 & 0 \\ 0 & b & 0 \\ 0 & 0 & c \end{bmatrix} \end{aligned} \quad (10)$$

and

$$\begin{aligned} &\lfloor\cdot\rfloor_S : \mathbb{R}_3 \to \mathbb{R}_{3\times3} \\ &\left\lfloor \begin{bmatrix} a \\ b \\ c \end{bmatrix} \right\rfloor_S = \begin{bmatrix} 0 & a & b \\ a & 0 & c \\ b & c & 0 \end{bmatrix}. \end{aligned} \quad (11)$$

To estimate the parameters of the matrix $\mathbf{A}$ a process alternating the estimation of $\mathbf{S}$ and $\mathbf{T}$ is used. Thus, assuming that the bias and the misalignment coefficients are known and applying Taylor formula for $\mathbf{A}$ on Equation 7, the scale parameters $\mathbf{S}$ are estimated from:

$$\begin{aligned} &(\Gamma - \lfloor\mathbf{S}\rfloor_D)(\hat{\mathbf{m}}_{B_1} - \mathbf{b}_m) \\ &= \mathrm{R}_{B_1B_2}(\Gamma - \lfloor\mathbf{S}\rfloor_D)(\hat{\mathbf{m}}_{B_2} - \mathbf{b}_m) + o(\|\,\mathbf{S}\,\|) + o(\|\,\mathbf{T}\,\|). \end{aligned} \quad (12)$$

where $\mathbf{I}_3 - \lfloor\mathbf{T}\rfloor_S$ is written Γ.

Since $\lfloor\mathbf{S}\rfloor_D\mathbf{K} = \lfloor\mathbf{K}\rfloor_D\mathbf{S}$ for any vector $\mathbf{K}$ of size 3 and $o(\|\,\mathbf{S}\,\|)$ and $o(\|\,\mathbf{T}\,\|)$ are negligible, Equation 12 is simplified as follows:

$$\begin{aligned} &\lfloor\mathrm{R}_{B_1B_2}(\hat{\mathbf{m}}_{B_2} - \mathbf{b}_m) - (\hat{\mathbf{m}}_{B_1} - \mathbf{b}_m)\rfloor_D\mathbf{S} \\ &= \mathrm{R}_{B_1B_2}\Gamma(\hat{\mathbf{m}}_{B_2} - \mathbf{b}_m) - \Gamma(\hat{\mathbf{m}}_{B_1} - \mathbf{b}_m) \end{aligned} \quad (13)$$

As for the bias, $\mathbf{S}$ can be estimated by resolving a linear system obtained by concatening Equation 13 for all the collected pairs of magnetic data. The rotation angle between two magnetic measurements that optimally constraints the scale estimation is $\theta_s^{opt} = \frac{\pi}{2}$. In fact for this angle value (assuming that the bias and the misalignement are perfectly known) the ratio between the norm of the two magnetic measurements is approximatively equal to the ratio of the scales. As for the bias estimation Equation 13 is weighted by $\exp(-\frac{(\theta_s^{opt}-\theta_{\mathrm{R}_{B_1B_2}})^2}{\Theta^2})$.

Following the same procedure as for the scale parameters, the misalignement coefficients $\mathbf{T}$ are obtained by :

$$\begin{aligned} &\lfloor\mathrm{R}_{B_1B_2}(\hat{\mathbf{m}}_{B_2} - \mathbf{b}_m) - (\hat{\mathbf{m}}_{B_1} - \mathbf{b}_m)\rfloor_S\mathbf{T} \\ &\simeq \mathrm{R}_{B_1B_2}\Upsilon(\hat{\mathbf{m}}_{B_2} - \mathbf{b}_m) - \Upsilon(\hat{\mathbf{m}}_{B_1} - \mathbf{b}_m) \end{aligned} \quad (14)$$

As the misalignment corresponds to the angle between the real sensor frame and the frame B_i, it is similar to a supplementary bias that varies depending on the measured magnetic field. Its observability is thus maximal when $\theta_t^{opt} = \pi$. As for the bias estimation Equation 14 is weighted by $\exp(-\frac{(\theta_t^{opt}-\theta_{\mathrm{R}_{B_1B_2}})^2}{\Theta^2})$.

For the experiments, we chose $\Theta = 1$ radian as the weights must be low when the values are far from the optimal angle difference, while still being sufficiently high for pairs relatively close to the angle difference. Nonetheless, this value may be changed depending on the collected data.

3) Stopping criterion on data acquisition: To ensure accurate estimation of the calibration parameters, there must be sufficient pairs of magnetic measurements for which the associated rotation $\mathbf{R}_{B_1B_2}$ forms an angle close to the optimal observability angle of the bias and the scale-misalignment matrix.

The criterion we propose to stop the acquisition of magnetic data for the magnetometer calibration is thus based on the number of equations with high observability of the calibration parameters. A pair of magnetic measurements satisfy this criteria if:

$$abs(\theta_{\mathrm{R}_{B_1B_2}} - \theta_j^{opt}) < \delta_j \quad (15)$$

with δ_j a threshold. j is equal to b, s or t (for the bias, the scale and the misalignment).

The smaller δ_j is, the lower the noise is in the selected equations. However, it is difficult to obtain two values at close locations with the perfect angle difference. As a relatively large number of equations is needed to obtain an accurate estimation, the tolerance threshold should be quite large. Later, for the experiments, the values are set to $\delta_b = \delta_t = \frac{\pi}{2}$ and $\delta_s = \frac{\pi}{4}$.

C. Second step of our calibration process: calibration refinement through non linear optimization

The second step of our calibration process refine the coarse calibration obtained during the first step by simultaneously estimating the magnetic field. We use Gaussian Process modelization of the magnetic field describe in Section III-B.

The cost function to miminize is defined by the errors between the collected magnetic measurements and the prediction vector $\mathbb{E}[B(\mathbf{p})]$:

$$c = \| \mathbb{E}[B(\mathbf{p})] - vec\Big(\mathbf{R}_{GM}(\mathbf{A}^{-1}(\hat{\mathbf{m}}_\mathbf{n} - \mathbf{b}_m))\Big) \|^2 . \quad (16)$$

This equation can be reformulated like this :

$$c = \| (\nabla\Phi\Omega - \mathbf{I}_{3D})\mathrm{vec}(\mathbf{R}_{GM}(\mathbf{A}^{-1}(\hat{\mathbf{m}}_\mathbf{n} - \mathbf{b}_m))) \|^2 . \quad (17)$$

$\nabla\Phi = \nabla\Phi_*$ since the predicted measurements are done at the location of the collected data. $\nabla\Phi\Omega - \mathbf{I}_{3D}$ is constant and can be precalculated once for all. This equation depends only of the calibration parameters $s_1, s_2, t_1, t_2, t_3, b_m$. s_3 is fixed to the value that was obtained outdoor, since indoors, the scale matrix is observable up to an unknown scale factor. Equation 17 is optimized by the Levenberg-Marquadt algorithm. There is no guarantee that this algorithm would not converge to local minima. However, on all the experiments that we performed, it always converged to the correct calibration, as the magnetometer was moved in a lot of different directions (see Section IV-B3). Inaccurate calibration results are mostly due to an insufficient exploration of the different rotation angles of the magnetometer.

V. EXPERIMENTS

In this section, the proposed calibration process is evaluated. After a brief description of the acquisition system, our approach is compared with state of the art magnetometer calibration methods. In addition to the classical comparison of calibration matrices with a ground truth, we also evaluate the accuracy of a magnetic field-based SLAM algorithm depending on the magnetometer calibration quality.

A. Experimental setup

Our acquisition platform is composed of a helmet with 4 FLIR Blackfly S cameras and an SBG-Ellipse-N sensor that contains an IMU and a magnetometer (whose axes are aligned with those of the IMU). All the sensors are rigidly mounted and their data are synchronized. The 4 cameras and the IMU are calibrated using the software Kalibr [16]. The cameras are disposed in two pairs: one stereo pair in front and another one in the rear of the helmet.

B. Evaluation of the proposed magnetometer calibration algorithm

To evaluate the proposed magnetometer calibration on a representative dataset, we use 4 different sequences. For the Sequences 1 and 2, the magnetometer is rotated in all directions, in an area as small as possible (i.e. with as little translational movements as possible). For these two sequences, the magnetic field variations are small. For the Sequences 3 and 4, the helmet is rotated in a wider area, of size 5 m $\times$ 5 m $\times$ 5 m. The duration of all these sequences is limited to 30 s, to demonstrate that the magnetometer calibration can be achieved online in a reasonable time during an initialization phase of a magnetic field-based SLAM algorithm. The quality of the estimated bias and scale-misalignemet matrices are evaluated by $err_\mathbf{b} = \| \mathbf{b} - \mathbf{b}_{ext} \|$ and $err_\mathbf{A} = \left[\sum_{i=1}^{3} \sum_{j=1}^{3} (\mathbf{A}\mathbf{A}_{ext}^{-1} - \mathbf{I}_3)_{i,j}^2 \right]^{\frac{1}{2}}$ where $\mathbf{A}_{ext}$ et $\mathbf{b}_{ext}$ are the ground truth calibration matrices obtained from an outdoor calibration [5] performed just before each sequences.

To make sure that our method can be used in various types of indoor environments, the areas where the calibrations were performed were filled with various objects. Figure 2 is a picture of one of them. The ground truth magnetic field is obtained applying to the raw measurements the ground truth calibration (the outdoor calibration) and rotating all of them to the same referential. The noise of the sensor is neglected: its amplitude is about 0.3μT for the sensor used in the experiments. It would not change the overall map profile. The magnetic field is spatially very contrasted, especially on the y-axis: on a distance of 10 cm, a difference of 15 μT is observed. According to [1], the effect on the magnetic field of small metallic objects, such as watches or computers, decreases strongly with the distance. The range is about 30 cm for a laptop. An elevator, on the contrary, has a perturbation range of a few meters. Therefore in most indoor environments the main perturbations of the magnetic field are caused by the metallic structure of the building: the objects in the room have a very limited influence on the calibration, as long as the system is not very close to them. However, our method would lose in accuracy if the calibration is close to an elevator that is moving between several floors, as the temporal variations of the field are no longer negligible.

According to [10], the local magnetic field for small volumes can be considered to be constant. In our experiments, this approximation is only true for the first sequence on which an ellipsoid fitting calibration algorithm with a scaling constraint perfomed relatively well ($err_\mathbf{A} = 0.795\mu$T and $err_\mathbf{A} = 2.733.10^{-2}$). However, this assumption is not verified for all others Sequences. As illustrated in Figure 3, the collected magnetic data of Sequence 2 form approximately a half-ellipsoid, but many outliers are present which results a poor calibration estimate. The bias estimated on this sequence with [5] is aberrant ($err_\mathbf{A} > 100\mu$T).

Therefore we only compare the proposed calibration method with our implementation of the state of the art indoor calibra-

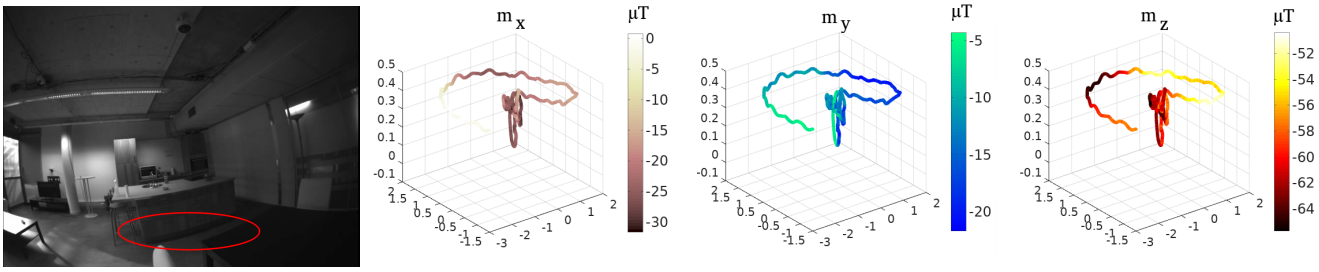

(a) Studied area

(b) The three components of the ground truth magnetic field

Fig. 2. Studied area for Sequence 3 of Table II and the corresponding ground truth magnetic field for the calibration trajectory in that area.

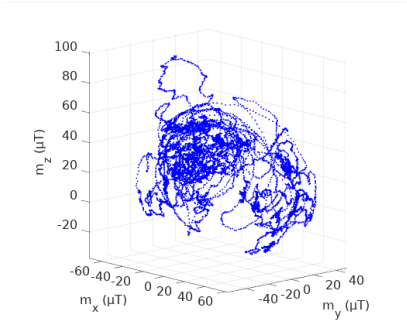

Fig. 3. Collected magnetic data on Sequence 2.

tion method [7] that is robust to magnetic field variations. For the latter, we used 27 control points for the spline model on the four sequences, as the explored areas are all relatively small. For our method, 27 eigenfunctions are used for the GP model.

Table I presents the comparison of our magnetometer calibration process with the state of the art indoor calibration algorithm [7] on the four sequences described above. Our method reaches better precisions: on the four sequences, the bias estimation improvement is of 46% on average and of 36% for the scale-misalignment matrix. In particular for Sequence 3, the bias estimation of [7] lacks of precision, with an error of 3.657μT. With the proposed approach, the error of the estimated bias is below 1μT.

C. Influence of magnetometer calibration errors on magnetic field-based SLAM

In this section we evaluate the impact of the magnetometer calibration on the accuracy of a magnetic field-based SLAM algorithm [3]. For this purpose, different runs are performed on the same sequences with a magnetic calibration obtained by our approach, the one of [7] and an outdoor calibration. The SLAM algorithm of [3] uses visual inertial odometry and maps the magnetic field online with a Gaussian Process. The magnetic data are fused with the visual inertial odometry via a particle filter to reduce the drift when the trajectory passes through a location already mapped. The two sequences used for evaluation are composed of two parts. During the first thirty seconds the acquisition system is moved and rotated in all directions. The localization is achieved by visual-inertial odometry and the magnetometer calibrated with one of the methods described above (except for the outdoor calibration). Then a trajectory is performed by walking in several corridors in both directions. The SLAM algorithm [3] is used for localization, mapping the magnetic field online. For the run with the calibration performed outdoor, the modeling of the magnetic field also begins after the first 30 seconds so that the comparison of the estimated trajectories is fair. Figure 4 represents the SLAM trajectories obtain with the different magnetometer calibrations for one of the two sequences. The environment explored during the calibration phase for the first sequence in Table II is part of a small office lounge, as can be seen on Figure 5. The initialization of Sequence 2 was obtained in the same area as Sequence 3 in Table I.

The different executions are compared in terms of position and rotational errors. The Absolute Translation Error (ATE) is defined as $e = \sqrt{\frac{1}{n}\sum_{j=1}^{n} ||\mathbf{t}_{GI}^{j} - \hat{\mathbf{t}}_{GI}^{j}||^2}$ with n the total number of data. The rotational errors are composed of two components: $e_{azimuth} = \sqrt{\frac{1}{n}\sum_{j=1}^{n} |(R_{GI}^{j} \ominus \hat{R}_{GI}^{j})_z|^2}$ and $e_{leveling} = \sqrt{\frac{1}{n}\sum_{j=1}^{n} ||(R_{GI}^{j} \ominus \hat{R}_{GI}^{j})_{xy}||^2}$, with $\ominus : SO(3) \times SO(3) \to \mathbb{R}^3$, $R_1 \ominus R_2 = \log_{SO(3)}(R_1 R_2^{\top})$. $\mathbf{t}_{GI}$ and $\mathbf{R}_{GI}$ correspond to the ground truth positions and rotations and $\hat{t}_{GI}$ and $\hat{R}_{GI}$ are the ones estimated by the magnetic field-based SLAM algorithm. The ground truth are obtained by the VISLAM algorithm [15] with loop closure and global bundle adjustment as post processing.

Table II presents the localization errors for the different runs. The localization accuracy of the magnetic-field based SLAM is better on all the sequences when a proper calibration is used compared to visual-inertial odometry. The ATE error on average, when our calibration or an outdoor calibration is used, is 52% more precise. The leveling error on average, compared to visual-inertial odometry (VIO), is lower by 77% when our magnetometer calibration is used.

However, with a poorer magnetometer calibration, such as the one obtained with [7] or an outdated one, the gain in localization accuracy compared to a VIO algorithm is weaker and may sometimes be deteriorated. For example, for the second sequence, the ATE increases of 117% when an outdated calibration is used. This demonstrates that the calibration must be reestimated regularly. Therefore it is important to have an easily deployable solution for recalibration.

		Sequence 1	Sequence 2	Sequence 3	Sequence 4
[7]	$err_{\mathbf{b}}$	0.674	1.040	3.657	0.945
	$err_{\mathbf{A}}$	$6.819.10^{-2}$	$4.363.10^{-2}$	$\mathbf{3.689.10^{-2}}$	$\mathbf{6.669.10^{-2}}$
Our method Section IV	$err_{\mathbf{b}}$	**0.384**	**0.673**	**0.862**	**0.647**
	$err_{\mathbf{A}}$	$\mathbf{1.041.10^{-2}}$	$\mathbf{2.050.10^{-2}}$	$6.090.10^{-2}$	$9.095.10^{-2}$

TABLE I

COMPARISON OF THE CALIBRATION ACCURACY OBTAINED WITH DIFFERENT METHODS.

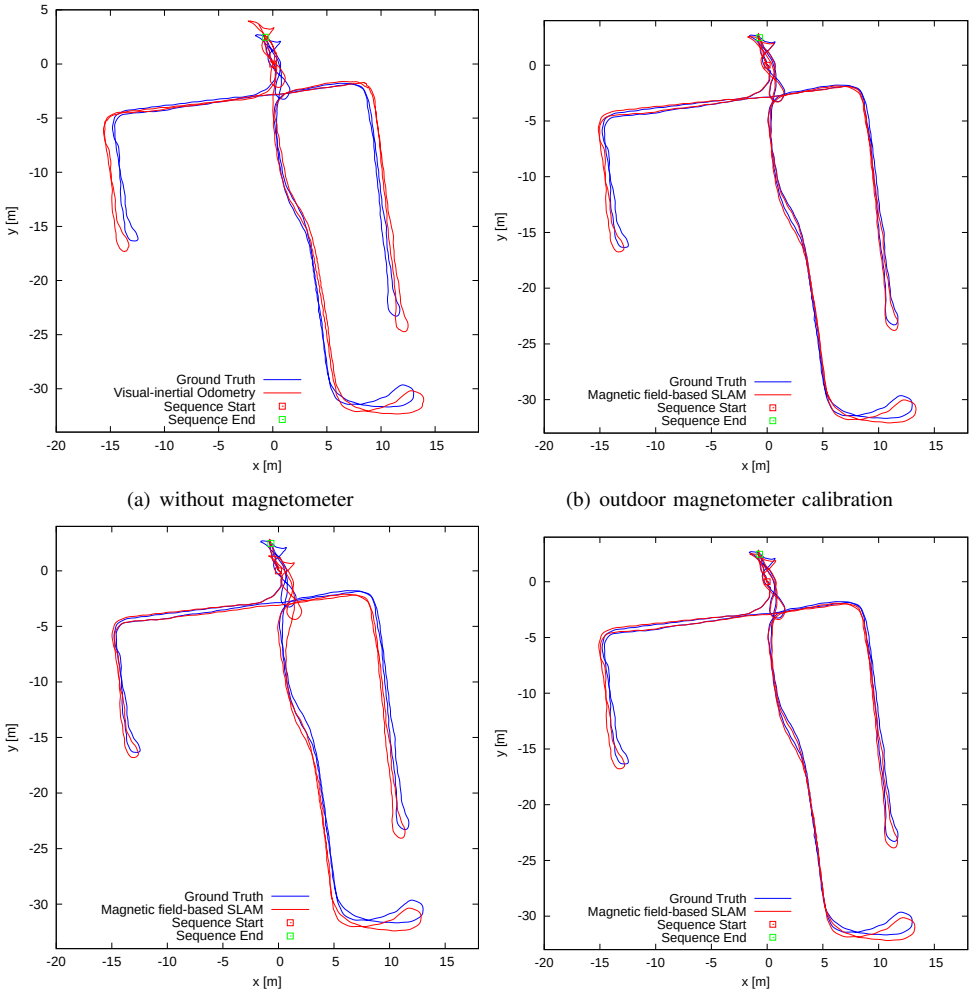

(a) without magnetometer

(b) outdoor magnetometer calibration

(c) magnetometer calibration [7]

(d) proposed magnetometer calibration

Fig. 4. Executions of a magnetic field-based SLAM algorithm with different magnetometer calibrations (Sequence 1 of Table II). The ground truth trajectory is represented in blue and the SLAM trajectories in red. Top Left: The magnetic data are not used and the SLAM algorithm [3] behaves like visual-inertial odometry.

Fig. 5. Area where the calibration is performed for Sequence 1 in Table II.

The processing time of our calibration method, for 30 s of magnetic data acquisition at 50 Hz is about 600 ms. Our method is thus well suited to calibrate online a magnetometer for magnetic field-based SLAM algorithm.

VI. CONCLUSION

In this paper, we present an algorithm for magnetometer calibration in indoor environments. It is based on the joint estimation of calibration matrices and a Gaussian process model by a two-step optimization algorithm.

Experimental results have shown that our solution provides an accurate and efficient calibration of the magnetometer. It

Sequence number		Sequence 1 (5 min 44, 309 m)	Sequence 2 (5 min 43, 251 m)
Visual-inertial odometry	ATE	0.905 m	0.326 m
	Leveling err.	0.758°	0.234°
	Azimuth err.	0.862°	1.494°
Magnetic field-based SLAM [3] calibration [7]	ATE	0.667 m	0.342 m
	Leveling err.	0.740°	0.220°
	Azimuth err.	0.747°	2.166°
Magnetic field-based SLAM [3] our calibration	ATE	0.371 m	**0.181 m**
	Leveling err.	0.103°	**0.085**°
	Azimuth err.	**0.363**°	1.499°
Magnetic field-based SLAM [3] outdoor calibration [5]	ATE	**0.352 m**	0.182 m
	Leveling err.	**0.068**°	0.091°
	Azimuth err.	0.449°	**1.421**°
Magnetic field-based SLAM [3] outdated outdoor calibration (5 months ago)	ATE	0.640 m	0.708 m
	Leveling err.	0.644°	0.323°
	Azimuth err.	1.116°	5.210°

TABLE II

ATE, LEVELING AND AZIMUTH ERRORS OF MAGNETIC FIELD-BASED SLAM ALGORITHM, FOR DIFFERENT MAGNETIC CALIBRATIONS. THE RESULTS OF VISUAL-INERTIAL ODOMETRY ARE ALSO INDICATED.

enables online magnetometer calibration during an initialization phase of magnetic field-based SLAM algorithms. We also demonstrate in this paper the impact of magnetometer calibration errors on the localization accuracy of magnetic field-based SLAM algorithms.

REFERENCES

[1] B. Li, T. Gallagher, A. G. Dempster, and C. Rizos, "How feasible is the use of magnetic field alone for indoor positioning?" in *IPIN*, November 2012.

[2] I. Vallivaara, J. Haverinen, A. Kemppainen, and J. Roning, "Magnetic field-based slam method for solving the localization problem in mobile robot floor-cleaning task," in *ICAR*, June 2011.

[3] M. Kok and A. Solin, "Scalable Magnetic Field SLAM in 3D Using Gaussian Process Maps," in *FUSION*, July 2018.

[4] J. Coulin, R. Guillemard, V. Gay-Bellile, C. Joly, and A. de La Fortelle, "Tightly-coupled magneto-visual-inertial fusion for long term localization in indoor environment," *IEEE Robotics and Automation Letters*, vol. 7, no. 2, pp. 952–959, April 2022.

[5] C. C. Foster and G. H. Elkaim, "Extension of a two-step calibration methodology to include nonorthogonal sensor axes," *IEEE Transactions on Aerospace and Electronic Systems*, vol. 44, no. 3, pp. 1070–1078, October 2008.

[6] J. F. Vasconcelos, G. Elkaim, C. Silvestre, P. Oliveira, and B. Cardeira, "Geometric Approach to Strapdown Magnetometer Calibration in Sensor Frame," *IEEE Transactions on Aerospace and Electronic Systems*, vol. 47, no. 2, pp. 1293–1306, April 2011.

[7] M. Muraccini, A. L. Mangia, M. Lannocca, and A. Cappello, "Magnetometer calibration and field mapping through thin plate splines," *Sensors*, vol. 19, no. 2, 2019, article number: 280.

[8] G. Troni and L. Whitcomb, "Adaptive Estimation of Measurement Bias in Three-Dimensional Field Sensors with Angular Rate Sensors: Theory and Comparative Experimental Evaluation," in *RSS*, June 2013.

[9] G. Fedele, L. D'Alfonso, and G. D'Aquila, "Magnetometer bias finite-time estimation using gyroscope data," *IEEE Transactions on Aerospace and Electronic Systems*, vol. 54, no. 6, pp. 2926–2936, May 2018.

[10] M. Kok and T. Schön, "Magnetometer Calibration Using Inertial Sensors," *IEEE Sensors Journal*, vol. 16, no. 14, pp. 5679–5689, May 2016.

[11] J. F. Vasconcelos, G. Elkaim, C. Silvestre, P. Oliveira, and B. Cardeira, "On Calibration of Three-Axis Magnetometer," *IEEE Sensors Journal*, vol. 15, no. 11, pp. 6424–6431, November 2015.

[12] B. Siebler, S. Sand, and U. D. Hanebeck, "Localization With Magnetic Field Distortions and Simultaneous Magnetometer Calibration," *IEEE Sensors Journal*, vol. 21, no. 3, pp. 3388–3397, February 2021.

[13] "EEE standard for specifying and testing single-axis interferometric fiber optic gyros," *IEEE Std 952-2020 (Revision of IEEE Std 952-1997)*, pp. 1–93, February 2021.

[14] A. Solin, M. Kok, N. Wahlström, T. Schön, and S. Särkkä, "Modeling and Interpolation of the Ambient Magnetic Field by Gaussian Processes," *IEEE Transactions on Robotics*, vol. 34, no. 4, pp. 1112—-1127, September 2015.

[15] C. Campos, R. Elvira, J. J. G. Rodriguez, J. M. M. Montiel, and J. D. Tardos, "ORB-SLAM3: An Accurate Open-Source Library for Visual, Visual–Inertial, and Multimap SLAM," *IEEE Transactions on Robotics*, vol. 37, no. 6, pp. 1874–1890, December 2021.

[16] J. Rehder, J. Nikolic, T. Schneider, T. Hinzmann, and R. Siegwart, "Extending *kalibr*: Calibrating the Extrinsics of Multiple IMUs and of Individual Axes," *ICRA*, May 2016.